Fuel 338 (2023) 127292

Contents lists available at ScienceDirect

Fuel

journal homepage: www.elsevier.com/locate/fuel

Full Length Article

Bubble dynamics and thermochemical characteristics of bubbling fluidized bed methanation

Dali Kong [a], Shuai Wang [a,*], Kun Luo [a,b], Jiahui Yu [a], Jianren Fan [a,b]

[a] State Key Laboratory of Clean Energy Utilization, Zhejiang University, Hangzhou 310027, China
[b] Shanghai Institute for Advanced Study of Zhejiang University, Shanghai 200120, China

ARTICLE INFO

Keywords:
CFD-DEM
Methanation
Bubble behaviours
Bubbling fluidized bed

ABSTRACT

Methanation is a promising technology to transform carbonaceous materials into high-value fuels, yet the relationship between multi-scale structures and reactor performance is still not well understood. Accordingly, the methanation process in a bubbling fluidized bed (BFB) reactor is investigated via the computational fluid dynamics-discrete element method (CFD-DEM) featuring thermochemical sub-models. A novel algorithm is developed for bubble identification and related information statistics. The effects of crucial operating parameters on bubble behaviours are quantified. Moreover, the underlying mechanism of mesoscale bubble behaviours is illuminated by linking with microscale particle dimensionless number and macroscale reactor performance. The results show that the bubble dynamics can be well captured by the novel bubble identification algorithm. Particle Reynolds number (Re_p) and Nusselt number (Nu_p) have the highest values in the bubble phase and the lowest values in the emulsion phase. Decreasing inlet gas velocity, increasing particle size, and lowering operating temperature causes smaller volume ratios of the bubble phase to emulsion phase, thereby enhancing interphase heat and mass transfer and promoting methane concentration in the gas products.

1. Introduction

Methane (CH_4) with the advantages of high calorific value, wide feedstock availability, and easy liquefaction has been extensively practised in energy industries, yet most methane consumed comes from fossil natural gas resources [1,2]. Climate change and energy depletion caused by increasing fossil fuel consumption call for efficient methanation [3,4]. Specifically, methanation is a thermochemical route converting gas mixture rich in CO and H_2 (usually the gasification products of biomass and coal) to methane-rich syngas, including two exothermic homogeneous reactions, i.e., methanation reaction and water–gas shift reaction, given by [5]:

$$CO + 3H_2 \leftrightarrow CH_4 + H_2O \quad \Delta H_R^0 = -206.28\ \mathrm{kJ/mol} \tag{R1}$$

$$CO + H_2O \leftrightarrow CO_2 + H_2 \quad \Delta H_R^0 = -41.16\ \mathrm{kJ/mol} \tag{R2}$$

Among all reactors to perform methanation, bubbling fluidized bed (BFB) is the best choice due to its advantages in wide fuel applicability, good operation flexibility, excellent temperature control, and especially good heat and mass transfer performance. However, the BFB reactor is a dense particulate-reacting system within multi-physics processes and multi-scale flow structures [6,7]. Specifically, the flow hydrodynamics, heat transfer, and chemical reactions inter-connect, meanwhile, microscale inter-particle/phase interactions, mesoscale bubble evolution, and macroscale reactor performance entangle, making it challenging for people to understand in-furnace phenomena. Among these complex mechanisms, the mesoscale bubble evolution (e.g., coalescence, growth, and bursting) as a typical feature of the BFB reactor links microscale particle behaviours with macroscale reactor performance. So far, substantial experimental efforts have been made to study BFB reactors for process design and optimization. However, the experimental method generally delivers macro-scale information in local positions or regions (e.g., product yields at the outlet, temperature distribution in the central line) [8–10] but is hard to capture the micro-scale information (e.g., particle collisions) and mesoscale information (e.g., bubble dynamics) in the whole reactor. Moreover, the trials and errors of experiment measurements are time-consuming and expensive.

As an alternative, numerical simulation is cost-effective, repeatable, and systematic to investigate dense particulate reacting processes such as methanation in the BFB reactor. Among the existing numerical methods, the two-fluid model based on the Eulerian-Eulerian framework treats both particles and fluid as interpenetrating continua and

* Corresponding author.
E-mail address: wshuai2014@zju.edu.cn (S. Wang).

https://doi.org/10.1016/j.fuel.2022.127292
Received 24 October 2022; Received in revised form 11 December 2022; Accepted 24 December 2022
Available online 2 January 2023

Nomenclature

$A_{p,i}$	Surface area of particle i, m^2
β	Interphase momentum exchange coefficient, $kg{\cdot}m^{-3}{\cdot}s^{-1}$
$C_{p,g}$	Specific heat capacity of the gas phase, $J{\cdot}kg^{-1}{\cdot}K^{-1}$
$C_{p,i}$	Specific heat capacity of particle i, $J{\cdot}kg^{-1}{\cdot}K^{-1}$
D_n	Diffusion coefficient of species n, $m^2{\cdot}s^{-1}$
$e_{n,ij}$	Normal coefficient of restitution, -
$\mathbf{f}_c$	Contact force exerted on a specific particle, N
$\mathbf{f}_d$	The gas force exerted on a specific particle, N
$\mathbf{f}_{cn,ij}$	Normal contact forces between particle i and j, N
$\mathbf{g}$	Gravitational acceleration, $m{\cdot}s^{-2}$
h_{pg}	Convective heat transfer coefficient, $W{\cdot}m^{-2}{\cdot}K^{-1}$
$\mathbf{I}_{gm}$	Inter-phase momentum exchange rate, $N{\cdot}m^{-3}$
I_p	Moment of inertia of a specific particle, $kg{\cdot}m^2$
k	The number of particles colliding with particle i
$k_{n,ij}$, $k_{t,ij}$	Normal and tangential spring coefficients, $N{\cdot}m^{-1}$
L	Distance from contact point to particle centre, m
l_{ij}	Distance between particles i and j, m
$\mathbf{n}_{ij}$	The normal unit vector between particle i and j, -
N_p	Particle number, -
$N_{p,\Omega}$	Particle number in the sub-domain Ω, -
$Nu_{p,i}$	Nusselt number of particle i, -
Pr	Prandtl number, -
q_{gp}	Gas-particle convective heat transfer rate, W
q_{pgp}	Particle-gas-particle conductive heat transfer rate, W
q_{pp}	Particle-particle conductive heat transfer rate, W
q_{rad}	Radiative heat transfer rate, W
R	Gas constant, $J{\cdot}mol^{-1}{\cdot}K^{-1}$
$R_{c,ij}$	The radius of the contact region, m
Re_p	Reynold number, -
R_{in}, R_{out}	Lower and upper bounds of conductive heat transfer region, m
$R_{p,i}$, $R_{p,j}$	The diameter of particles i and j, m
t	Time instant, s
$\mathbf{t}_{ij}$	Tangential unit vector between particle i and j, -
T_{env}	Environment temperature, K
T_{ref}	Reference temperature, K
T_g	Gas temperature, K
$T_{g,\Omega}$	Gas temperature in the sub-domain Ω, K
$T_{p,i}$, $T_{p,j}$	Temperatures of particles i and j, K
$\mathbf{u}_g$	Gas velocity vector, $m{\cdot}s^{-1}$
$\mathbf{v}_p$	Particle velocity vector, $m{\cdot}s^{-1}$
V_c	Cell volume, m^3
$V_{p,i}$	Particle volume, m^3
X_n	Mass fraction of n^{th} species, -

Greek symbols

ε_g	Void fraction, -
$e_{p,i}$	Particle emissivity, -
β	Interphase momentum exchange coefficient, $kg{\cdot}m^{-3}{\cdot}s^{-1}$
ΔH_{rg}	Heat source of the gas phase from chemical reactions, $W{\cdot}m^{-3}$
κ_g	Gas thermal conductivity, $W{\cdot}m^{-1}{\cdot}K^{-1}$
$\kappa_{p,i}$, $\kappa_{p,j}$	Thermal conductivity of particles i and j, $W{\cdot}m^{-1}{\cdot}K^{-1}$
$\eta_{n,ij}$, $\eta_{t,ij}$	Normal and tangential damping coefficients, $kg{\cdot}s^{-1}$
$\delta_{n,ij}$, $\delta_{t,ij}$	Normal and tangential overlap displacements, m
μ	Friction coefficient
μ_g	Gas viscosity, $kg{\cdot}m^{-1}{\cdot}s^{-1}$
ρ_g, ρ_p	Gas and particle density, $kg{\cdot}m^{-3}$
$\boldsymbol{\omega}_i$	Particle angular velocity, $rad{\cdot}s^{-1}$

Subscripts

g	Gas phase
i	Particle i
ij	Interactions between particles i and j
j	Particle j
n	Variables in the normal direction
p	Properties of the particle phase

Acronyms

BFB	Bubbling fluidized bed
CFD	Computational fluid dynamics
DEM	Discrete element method
LSD	Linear spring dashpot
CDS	Central difference scheme

simplifies inter-particle collisions [11]. This method with high computational efficiency has been widely employed to model fluidized bed systems with macro-scale information obtained [12–14]. Nevertheless, this method has inherent defects in capturing particle behaviours, e.g., particle collisions, rotation, and thermochemical behaviours [15]. In contrast, the computational fluid dynamics-discrete element method (CFD-DEM) under the Eulerian-Lagrangian framework regarding particles as a discrete phase and calculating inter-particle collisions directly delivers a better choice [16], which can capture detailed particle behaviours and underpin the fundamental understanding of the reactor from the microscale perspective [17]. Moreover, the thermochemical sub-models can be integrated into the CFD-DEM framework to study heat and mass transfer of dense particulate reactive flow [18–20]. Recently, CFD-DEM has been widely applied to model dense particulate reactive flow in BFB reactors. For example, Hwang et al. [21] explored the effects of fluidization number on gasification performance in a BFB reactor. They demonstrated that CO_2 began to generate in the lower part of the reactor when the fluidization number exceeded 3.6 while CO and H_2 concentrations and carbon conversion efficiency decreased with the increased fluidization number. Wang et al. [19] examined the sensitivity of the contact model in affecting the simulation efficiency of biomass gasification. They claimed that the contact model significantly affected the simulation efficiency but insignificantly influenced the product yields. Hu et al. [22] numerically investigated coal gasification in a pilot-scale BFB reactor. They pointed out that gas back-mixing played an important role in controlling gas combustion and bubble behaviours highly affected horizontal fuel mixing. Although these previous CFD-DEM studies provide meaningful information regarding the microscale particle behaviours and macroscale reactor hydrodynamics, the thermophysical properties of the mesoscale bubble phase and its relationships with thermochemical behaviours in the BFB reactor have not been reported.

A BFB reactor is commonly identified by two regions, i.e., a lower dense region and an upper dilute region. The flow regime in the dense region involves three phases, i.e., an emulsion phase with a high solid holdup, a bubble phase with a low solid holdup, and an intermedia phase with a moderate solid holdup. Among the three phases, the mesoscale bubble phase bridges microscale and macroscale information. Specifically, a bubble will be generated when the superficial gas velocity exceeds the minimum fluidization velocity. The bubble behaviours cause the chaotic motions of particles, which intensifies the gas-particle/particle–particle mixing and further determines the flow regime in the bed and the resulting fluidization quality [23,24]. Besides, the distribution of bubbles in the bed greatly affects the spatial distribution of temperature, gas component concentration, and reaction rate, thereby determining the overall reactor performance [25]. Therefore, it is of significance to unveil: (i) how operating conditions and particle properties influence the bubble behaviours and (ii) how the bubble

behaviours affect the thermochemical behaviours and the resulting reactor performance.

To fulfil this gap, the methanation process in a BFB reactor is simulated by the CFD-DEM with the fundamental study of the mesoscale bubble behaviours and their relationships with the microscale particle behaviours and macroscale reactor thermochemical characteristics. A novel bubble identification algorithm is proposed to quantify bubble properties. The paper is structured below: section 2 denotes the mathematical model, followed by model settings in section 3. Section 4.1 gives the model validation of the bubble identification algorithm and reaction kinetics. Section 4.2 presents the general flow patterns. Section 4.3 gives the spatial distribution of gas species and reaction rate. Sections 4.4 and 4.5 show the effects of operating parameters on bubble behaviours, followed by the analysis of the dimensionless number in different regions. The effects of bubble dynamics on thermochemical behaviours are presented in section 4.6, followed by the conclusion.

2. Mathematical model

The governing equations and thermochemical sub-models are given in this section. Subsequently, a novel algorithm for bubble identification is described, followed by the numerical scheme.

2.1. Governing equations

The gas phase is governed by:

$$\frac{\partial(\varepsilon_g\rho_g)}{\partial t}+\nabla\cdot(\varepsilon_g\rho_g\mathbf{u}_g)=0 \tag{1}$$

$$\frac{\partial(\varepsilon_g\rho_g\mathbf{u}_g)}{\partial t}+\nabla\cdot(\varepsilon_g\rho_g\mathbf{u}_g\mathbf{u}_g)=\nabla\cdot\bar{\bar{S}}_g-\varepsilon_g\nabla p_g+\rho_g\varepsilon_g\mathbf{g}-\sum_{m=1}^{M}\mathbf{I}_{gm} \tag{2}$$

$$\frac{\partial(\varepsilon_g\rho_g C_{p,g}T_g)}{\partial t}+\nabla(\varepsilon_g\rho_g\mathbf{u}_g C_{p,g}T_g)=\nabla\cdot(\varepsilon_g\kappa_g\nabla T_g)-Q_{gp}-\Delta H_{rg} \tag{3}$$

$$\frac{\partial(\varepsilon_g\rho_g X_n)}{\partial t}+\nabla\cdot(\varepsilon_g\rho_g\mathbf{u}_g X_n)=\nabla\cdot(\varepsilon_g\rho_g D_n\nabla X_n)+R_{gn} \tag{4}$$

where $\mathbf{u_g}$ is the gas velocity; $C_{p,g}$ is the gas specific heat capacity; X_n is the mass fraction of n^{th} species. ΔH_{rg} is the heat of reaction. R_{gn} is the generation or consumption rate of n^{th} gas species. The gas volume fraction ε_g, interphase momentum exchange term $\mathbf{I}_{gm}$, and interphase energy exchange term Q_{gp} are given by:

$$\varepsilon_g=1-\frac{1}{V_c}\sum_{i=1}^{N_p}V_{p,i}\ ;\ I_{gm}=\frac{1}{V_c}\sum_{i=1}^{N_p}f_{d,i}\ ;\ Q_{gp}=\frac{1}{V_c}\sum_{i=1}^{N_p}q_{gp,i} \tag{5}$$

where $V_{p,i}$ and V_c are the volume of i^{th} particle and computational cell, respectively. $\mathbf{f}_{d,i}$ is the gas force acting on i^{th} particle; $q_{gp,i}$ is the heat flux exchange of i^{th} particle.

The kinematic and energy balances of i^{th} particle are given by:

$$m_i\frac{d\mathbf{v}_i}{dt}=m_i\mathbf{g}+\mathbf{f}_{d,i}+\mathbf{f}_{c,i} \tag{6}$$

$$I_i\frac{d\boldsymbol{\omega}_i}{dt}=\sum_{j=1,j\neq i}^{k}(L\mathbf{n}\times\mathbf{f}_{ct,ij}) \tag{7}$$

$$m_i C_{p,i}\frac{dT_{p,i}}{dt}=q_{gp,i}+q_{pp,i}+q_{pgp,i}\ +\ q_{rad,i} \tag{8}$$

where m_i, $\mathbf{v}_i$, I_i, $\boldsymbol{\omega}_i$, and $T_{p,i}$ are the mass, translational velocity, moment of inertia, rotational velocity, and temperature of i^{th} particle, respectively. $q_{pp,i}$, $q_{pgp,i}$, $q_{gp,i}$, and $q_{rad,i}$ are heat fluxes of i^{th} particle due to particle–particle conduction, particle-gas-particle conduction, convection, radiation, and chemical reactions, respectively. The gas force $\mathbf{f}_{d,i}$ exerting on i^{th} particle is given by:

$$\mathbf{f}_{d,i}=-\nabla P_g(x_i)V_i+\frac{\beta V_i}{(1-\varepsilon_g)}(\mathbf{u}_g(x_i)-\mathbf{v}_p) \tag{9}$$

where β is the gas–solid momentum exchange coefficient, evaluated by the Gidaspow drag model [26]. The collision force $\mathbf{f}_{c,i}$ including the normal component $\mathbf{f}_{cn,i}$ and the tangential component $\mathbf{f}_{ct,i}$, is given by:

$$\mathbf{f}_c=\sum_{j=1,j\neq i}^{k}(\mathbf{f}_{cn,ij}+\mathbf{f}_{ct,ij}) \tag{10}$$

$$\mathbf{f}_{cn,ij}=-\left(k_{n,ij}\delta_{n,ij}-\eta_{n,ij}\dot{\delta}_{n,ij}\right)\mathbf{n}_{ij} \tag{11}$$

$$\mathbf{f}_{ct,ij}=\begin{cases}-\left(k_{t,ij}\delta_{t,ij}-\eta_{t,ij}\dot{\delta}_{t,ij}\right)\mathbf{t}_{ij} & \text{for } |\mathbf{f}_{ct,ij}|\leqslant\mu|\mathbf{f}_{cn,ij}|\\ -\mu|\mathbf{f}_{cn,ij}|\mathbf{t}_{ij} & \text{for } |\mathbf{f}_{ct,ij}|>\mu|\mathbf{f}_{cn,ij}|\end{cases} \tag{12}$$

The linear spring-dashpot (LSD) is adopted to solve inter-particle collisions, which has been proved to be more efficient than the non-linear Hertzian model with numerical accuracy guaranteed [19]. Specifically, for collisions between particles i and j, the normal damping coefficient $\eta_{n,ij}$ is given by:

$$\eta_{n,ij}=\sqrt{2k_{n,ij}m_{eff}}\ \frac{|\ln e_{n,ij}|}{\sqrt{\pi^2+\ln^2 e_{n,ij}}} \tag{13}$$

where $e_{n,ij}$ is the normal coefficient of restitution, given by:

$$e_{n,ij}=\exp\left(-\frac{\eta_{n,ij}t_{n,ij}^{col}}{2m_{eff}}\right) \tag{14}$$

where m_{eff} ($=m_i m_j/(m_i+m_j)$) is the effective mass of particles i and j. $t_{n,ij}^{col}$ is the collision time between particle i and j, given by:

$$t_{n,ij}^{col}=\pi\left(\frac{k_{n,ij}}{m_{eff}}-\frac{\eta_{n,ij}^2}{m_{eff}^2}\right)^{-1/2} \tag{15}$$

A similar expression can be written for the tangential damping coefficient.

2.2. Heat and mass transfer models

Three heat transfer modes are considered for the particles, i.e., convection, conduction, and radiation. The heat of reaction is not considered as particles do not react. Specifically, convection occurs between gas and particles due to the temperature difference and velocity difference. The convective heat flux is calculated by combining the temperature difference, particle surface area, and particle Nusselt number (Nu_p). Specifically, the Ranz-Marshall correlation is one of the most well-known correlations to calculate the Nu_p of a single particle derived by drop evaporation experiments [27]. After that, a series of empirical correlations featuring fluid-particle transport regarding Nu_p has been developed by many researchers, e.g., Li and Mason [28], Gunn [29], and Garcia-Gutierrez et al. [30]. For example, Lian et al. [31] conducted an excellent study of oxy-fuel combustion in a fluidized bed reactor using the Nu_p correlation proposed by Gunn [29]. Gutierrez et al. [30] derived a new Nu_p correlation using the sublimation of dry ice particles using a novel methodology based on a macro-TGA fluidized bed. Although these Nu_p correlations consider complex scenarios, the Ranz-Marshall correlation has still been extensively applied to simulate the thermal behaviours of solid particles in fluidized bed reactors due to its advantages of easy implementation and reasonable prediction [32–34]. Accordingly, we adopted this correlation in the simulation after the capacity assessment of several commonly used Nu_p correlations. The conduction includes two parts, the particle–particle conductive heat flux $q_{pp,i}$ and particle-gas-particle conductive heat flux $q_{pgp,i}$.

Table 1
Heat transfer modes and the relevant expressions.

Heat transfer modes	Expressions
Convection	$q_{gp,i} = h_{pg,i}A_{p,i}(T_g - T_{p,i})$
Conduction	$q_{pp,ij} = 4\frac{\kappa_{p,i}\kappa_{p,j}}{\kappa_{p,i}+\kappa_{p,j}}R_{c,ij}(T_{p,j} - T_{p,i})$
	$q_{pgp,ij} = \kappa_g(T_{p,j} - T_{p,i})\int_{R_{in}}^{R_{out}} \frac{2\pi r}{l_{ij} - \left(\sqrt{R_{p,i}^2 - r^2} + \sqrt{R_{p,j}^2 - r^2}\right)}dr$
Radiation	$q_{rad,i} = e_{p,i}A_{p,i}\sigma\left(T_{env}^4 - T_{p,i}^4\right)$
Parameters:	
Heat transfer coefficient	$h_{pg,i} = \mathrm{Nu}_{p,i}d_{p,i}/\kappa_g$
Particle Nusselt number	$\mathrm{Nu}_{p,i} = 2.0 + 0.6Re_{p,i}^{1/2}Pr^{1/3}$
Prandtl number	$Pr = \mu_g C_{p,g}/\kappa_g$
Contact radius	$R_{c,ij} = \sqrt{R_{p,j}^2 - \left(\frac{R_{p,j}^2 - R_{p,i}^2 + l_{ij}^2}{2l_{ij}}\right)^2}$
Environment temperature	$T_{env} = \varepsilon_g T_{g,\Omega} + (1-\varepsilon_g)\frac{1}{N_{p,\Omega}}\sum_{j=1,j\neq i}^{N_{p,\Omega}} T_j$

The latter is calculated via assuming the heat flux is transferred through a gas layer wrapping the particle with a default thickness of 0.2 d_p [35]. The radiative heat transfer $q_{rad,i}$ plays a significant role at high temperatures (>600 °C), which is calculated by the temperature difference between i^{th} particle and the environment. Table 1 presents the heat transfer modes and the relevant expressions.

The methanation process in the BFB reactor involves the methanation reaction (R1) and water–gas shift reaction (R2), given by:

$$CO + 3H_2 \leftrightarrow CH_4 + H_2O \quad \Delta H_R^0 = -206.28\ \mathrm{kJ/mol} \tag{R1}$$

$$CO + H_2O \leftrightarrow CO_2 + H_2 \quad \Delta H_R^0 = -41.16\ \mathrm{kJ/mol} \tag{R2}$$

The reaction rates of the two reactions are formulated by the following reaction kinetics [36,37]:

$$r_{METH} = \frac{k_{METH}K_C\left(p_{CO}p_{H_2}^3 - p_{CH_4}p_{H_2O}/K_{METH}\right)}{p_{CO}^{0.5}p_{H_2}^{2.5}\left(1 + K_C p_{CO}^{0.5} + K_{OH}p_{H_2O}p_{H_2}^{-0.5}\right)^2} \tag{16}$$

$$r_{WGS} = \frac{k_{WGS}\left(p_{CO}p_{H_2O} - p_{CO_2}p_{H_2}/K_{WGS}\right)}{p_{H_2}^{0.5}\left(1 + K_C p_{CO}^{0.5} + K_{OH}p_{H_2O}p_{H_2}^{-0.5}\right)^2} \tag{17}$$

where r_{METH} is the rate of methanation reaction, r_{WGS} is the rate of water–gas shift reaction. r_{METH} and r_{WGS} are the reaction kinetic constants; K_{METH} and K_{WGS} denote the reaction equilibrium constants; K_C and K_{OH} are the adsorption equilibrium constants. They are expressed as:

$$k_{METH} = 1.16\exp\left[\frac{74100}{RT_{ref}}\left(1 - \frac{T_{ref}}{T_g}\right)\right]\ \mathrm{mol{\cdot}s^{-1}{\cdot}kg_{catalyst}^{-1}{\cdot}bar^{-0.5}} \tag{18}$$

$$k_{WGS} = 2.43\exp\left[\frac{154200}{RT_{ref}}\left(1 - \frac{T_{ref}}{T_g}\right)\right]\ \mathrm{mol{\cdot}s^{-1}{\cdot}kg_{catalyst}^{-1}{\cdot}bar^{-0.5}} \tag{19}$$

$$K_{METH} = 2.52\times10^6\exp\left[-\frac{223100}{RT_{ref}}\left(1 - \frac{T_{ref}}{T_g}\right)\right]\ \mathrm{bar^{-2}} \tag{20}$$

$$K_{WGS} = 29.2\exp\left[-\frac{38940}{RT_{ref}}\left(1 - \frac{T_{ref}}{T_g}\right)\right] \tag{21}$$

$$K_C = 1.77\exp\left[-\frac{61000}{RT_{ref}}\left(1 - \frac{T_{ref}}{T_g}\right)\right]\ \mathrm{bar^{-0.5}} \tag{22}$$

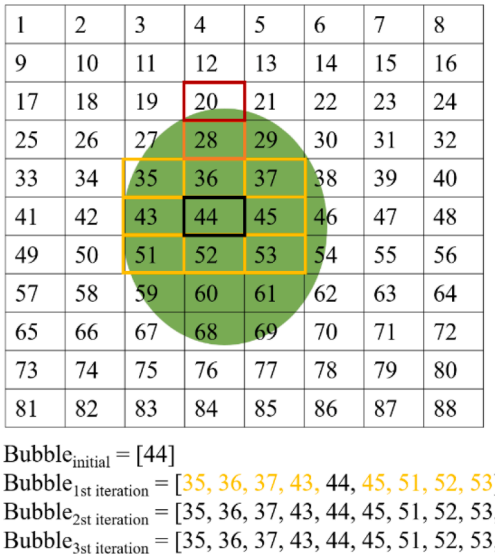

Fig. 1. The schematic representation of the bubble identification algorithm.

$$K_{OH} = 0.66\exp\left[-\frac{72300}{RT_{ref}}\left(1 - \frac{T_{ref}}{T_g}\right)\right]\ \mathrm{bar^{-0.5}} \tag{23}$$

where R is the gas universal constant. T_{ref} is the reference temperature.

2.3. Bubble identification algorithm

Bubbles will be generated in the BFB reactor when the superficial gas velocity exceeds the minimum fluidization velocity (U_{mf}). Li et al. [32] numerically investigated the methanation process in a bubbling fluidized bed (BFB), and they developed an approximate image processing method (AIPM) to study bubble properties, by which the bubble can be located, measured, and tracked. The results of bubble properties and reaction behaviours were in good agreement with the correlations from the literature and the experimental data, respectively. However, the thermal properties (e,g., gas species, temperature) of the bubbles in the system were unavailable by the AIPM. Yang et al. [25] numerically investigated biomass gasification in a BFB, and they studied the impact of the particle size distribution of sand material on the thermodynamic properties of the rising bubbles. The bubble was identified by at least 10 neighbouring computational cells. Unfortunately, the detailed bubble detection algorithm was unavailable, and the accuracy in describing bubble characteristics (e.g., volume, shape, and temperature) needs to be further verified. In the present work, a novel algorithm is developed for bubble identification and related information statistics. Compared with previous studies, the proposed bubble identification algorithm can efficiently and accurately describe bubbles in the BFB reactor, with abundant physical-thermal-chemical properties of bubbles obtained. The details of the bubble identification algorithm are given below.

The boundary of the bubble can be identified as an isosurface with a threshold voidage (ε_g) of 0.6 ~ 0.8 [38,39]. In this work, the voidage of 0.8 is adopted to identify the boundary of the bubble. Technically, the bubble is represented by many neighbouring cells with a voidage larger than the threshold value. The main idea is illustrated as follows:

a) The computational cells with a voidage >0.8 in the domain are retrieved and put in the vector Cell_{bub}.
b) A search process is then performed on each cell in the vector Cell_{bub}.
c) For cell i in the Cell_{bub}: ① Put the neighbouring cells of cell i in Cell_{bub} into the vector Bub_i. ② Employ the neighbouring cells in the set Bub_i as new starting cells to continue searching the corresponding

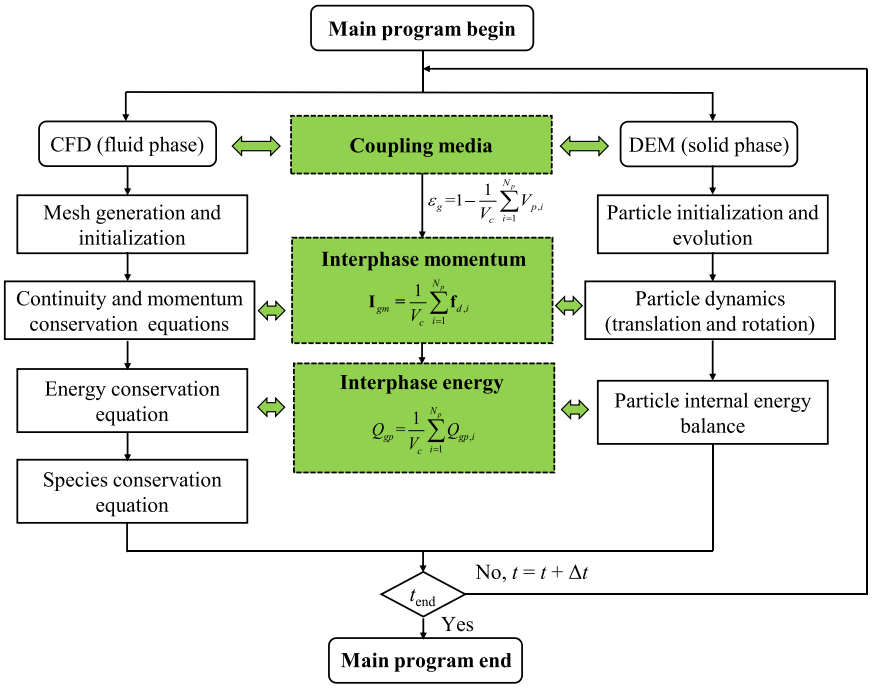

Fig. 2. The coupling procedure of the CFD-DEM approach.

neighbouring cells, until the number of cells in the set does not increase; ③ Delete the duplicate cells in the vector Bub_i.

d) In the subsequent searches, the cell will be skipped if cell *k* has been already contained in a bubble.

Fig. 1 shows the schematic representation of the bubble identification algorithm. Specifically, the voidage of the cells with the specific label 35, 36, 37, 43, 44, 45, 51, 52, 53, 28, and 20 reaches the threshold value. Taking cell 44 as the initial one, the neighbouring cells 35, 36, 37, 43, 45, 51, 52, and 53 are put into the vector Bub. Continuing searching the neighbouring cells based on these known cells, cell 28 meets the requirement and is put into the vector Bub. Similarly, based on cell 28, cell 20 is found and put into the vector Bub. After several iterations, the cells that represent the bubble can be found and detailed bubble information can be gained.

Based on the abovementioned bubble identification algorithm, the bubble size is calculated as follows [40]:

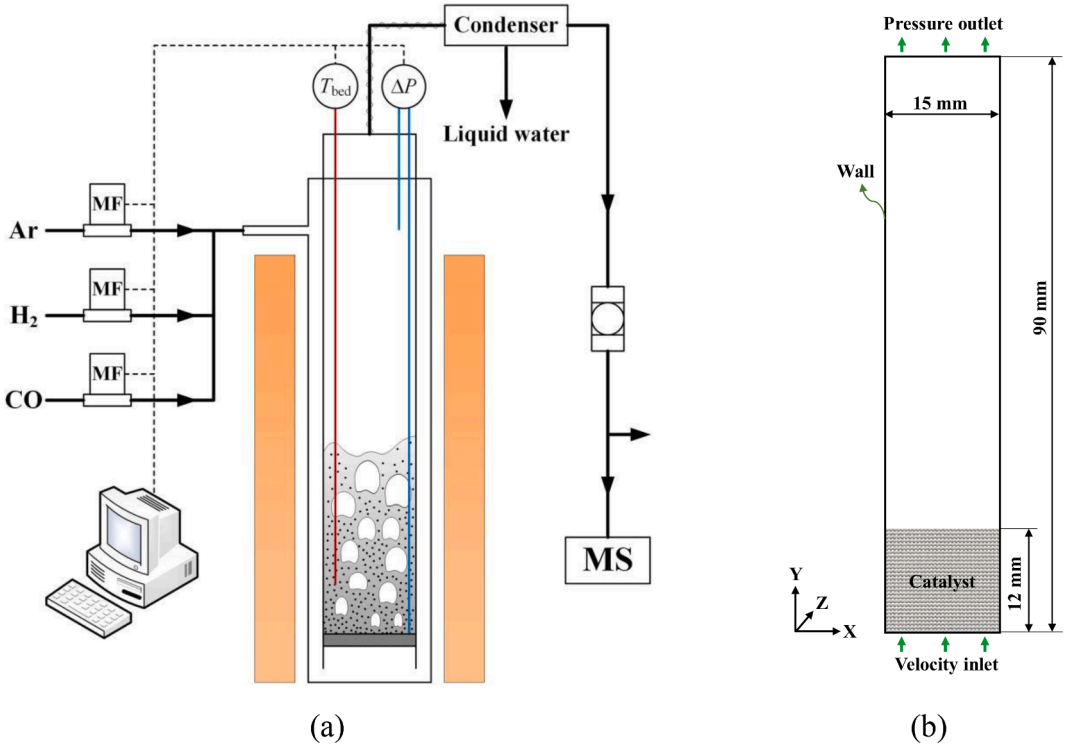

Fig. 3. The investigated BFB reactor: (a) experiment test-rig [36]; (b) current simulation.

$$d_b = \sqrt{4A_b/\pi} \tag{24}$$

where A_b is the bubble surface area, given by:

$$A_b = \sum_{i=1}^{N_{cell}} A_{cell,i}\varepsilon_{cell,i} \tag{25}$$

where N_{cell} represents the total number of cells occupied by the bubble. $A_{cell,i}$ is the area of the i^{th} cell, which is the product of the length of the i^{th} cell in X and Y directions. $\varepsilon_{cell,i}$ is the voidage of the i^{th} cell.

The central coordinate of the bubble is calculated by averaging the coordinate of all the computational cells occupied by the bubble:

$$C_b = \frac{1}{N_{cell}} \sum_{i=1}^{N_{cell}} C_{cell,i} \tag{26}$$

where C_b is the coordinate of the bubble. $C_{cell,i}$ is the coordinate of the i^{th} cell.

2.4. Numerical scheme

Fig. 2 shows the coupling procedure of the gas and solid phases. Specifically, the gas phase and solid phase involving kinematics, heat transfer, and mass transfer are governed by the corresponding equations. For the gas phase, the governing equations involving mass, momentum, energy, and species conservation are discretized. The transient term is discretized by a first-order implicit Euler scheme. The convection and diffusion terms are discretized by a second-order central difference scheme (CDS). The pressure–velocity coupling is treated by a SIMPLE algorithm. For the solid phase, the governing equations of particles involving physical and thermochemical properties are integrated explicitly by a first-order scheme. The collisions are solved by a soft-sphere contact model. Interphase coupling is solved via the voidage, inter-phase interaction, and heat transfer items.

The time step for the gas phase is controlled by the CFL:

$$\mathrm{CFL} = \Delta t_{\mathrm{CFD}} \max\left(\frac{|\mathbf{u}_f|}{\Delta x}\right) < 1 \tag{27}$$

where Δx is the cell size. The solid time step is defined as 1/50 of the minimum collision time, which is defined as:

$$t_{n,ij}^{col} = \pi\left(\frac{k_{n,ij}}{m_{eff}} - \frac{\eta_{n,ij}^2}{m_{eff}^2}\right)^{-1/2} \tag{28}$$

where k_n, η_n, m_{eff} are the particle properties.

3. Simulation settings

A lab-scale BFB reactor is used, referring to the experimental test rig from Li et al. [36], as shown in Fig. 3(a). A quasi-3D model is established to reduce computational costs [15,18]. This strategy has been broadly adopted to model fluidized beds [41,42]. For example, Li et al. [32] found that bubble dynamics in a simplified quasi-3D BFB measured by an approximate image processing method (AIPM) agreed well with the empirical correlations. Via experimentally studying bubble dynamics in a simplified quasi-3D BFB for different bed aspect ratios, Laverman et al. [40] demonstrated the correlation between the bubble rise velocity and the equivalent bubble diameter strongly depended on the bed width but does not depend on the bed height at the same bed width. Accordingly, a simplified quasi-3D BFB reactor used in this work is reasonable to present the physical-thermal-chemical behaviours of bubbles under the given conditions.

As shown in Fig. 3(b), the width, height, and depth of the BFB reactor are 15 mm, 90 mm, and 0.5 mm, respectively. Initially, the catalyst particles are packed at the lower region with 12 mm in height. Catalyst particles presented in the BFB reactor act as bed materials for fluidization and catalysts for improving reactions. There are no sand or biomass particles in the system, as methanation is a thermochemical route converting gas mixture (e.g., CO and H_2) to methane-rich syngas, including two exothermic homogeneous reactions. Initially, the reactor is filled with Argon (i.e., Ar). CO, H_2, and Ar are fed into the reactor from the bottom with the mole fractions of 0.2, 0.6, and 0.2, respectively. For the velocity, the walls are assigned as a non-slip boundary condition; for the temperature, the walls are specified as a constant temperature boundary condition. The operating temperature and pressure are 400 °C and 101325 Pa, respectively. The particle size is 0.125 mm, and the inlet gas velocity is 0.165 m/s. The grid size is 0.5 mm, which satisfies the demand of CFD-DEM calculation that the grid size should be 3 ~ 5 times the particle size to ensure numerical accuracy and stability [43]. Table 2 lists the detailed operating parameters and thermophysical properties of the catalyst particles. Specifically, the thermal conductivity and specific heat capacity are 10 $W{\cdot}m^{-1}{\cdot}\,K^{-1}$ and 1000 $J{\cdot}kg^{-1}{\cdot}\,K^{-1}$, respectively.

Table 2
Operating parameters and particle properties of the base case.

Parameters	Value	Unit
Bed size (x, y, z)	15 × 90 × 0.5	mm
Cell size	0.5	mm
Operating temperature	673	K
Operating pressure	101,325	Pa
Particle size	0.125	mm
Particle density	1680	$kg{\cdot}m^{-3}$
Inlet gas velocity	0.165	$m{\cdot}s^{-1}$
Initial inventory height	12	mm
Particle emissivity	0.7	–
Particle spring stiffness	1000	$N{\cdot}m^{-1}$
Particle restitution coefficient	0.9	–
Particle friction coefficient	0.3	–
Particle thermal conductivity	10	$W{\cdot}m^{-1}{\cdot}\,K^{-1}$
Particle specific heat capacity	1000	$J{\cdot}kg^{-1}{\cdot}\,K^{-1}$

Table 3
Operating parameters in the present study.

Number	T_0 (K)	U_g (m/s)	d_p (mm)
Case 1 (base case)	673	0.165	0.125
Case 2	623	0.165	0.125
Case 3	723	0.165	0.125
Case 4	673	0.125	0.125
Case 5	673	0.205	0.125
Case 6	673	0.165	0.1
Case 7	673	0.165	0.15

Thermophysical properties are determined according to the thermal database [44,45]. The simulation cases run on a cluster outfitted with 64 CPU processors. The time step is set to 1×10^{-5} s, and each case runs for about 7 days using 16 CPU processors to complete the simulation with a physical time of 15 s. Different operating parameters (e.g., particle size, inlet gas velocity, operating temperature) are employed to study the influence of these variables on the bubble properties and thermochemical behaviours. Table 3 summarizes the detailed operating parameters. Specifically, the operating temperature is set as 623 K, 673 K, and 723 K, respectively; the inlet gas velocity is specified as 0.125 m/s, 0.165 m/s, and 0.205 m/s, respectively; the particle size is assigned as 0.1 mm, 0.125 mm, and 0.15 mm, respectively.

4. Results and discussion

4.1. Model validation

The CFD-DEM approach has been well-validated in terms of hydrodynamics and heat transfer in our previous publications [16,18]. In this section, the bubble identification algorithm and reaction kinetics are validated with the experimental data.

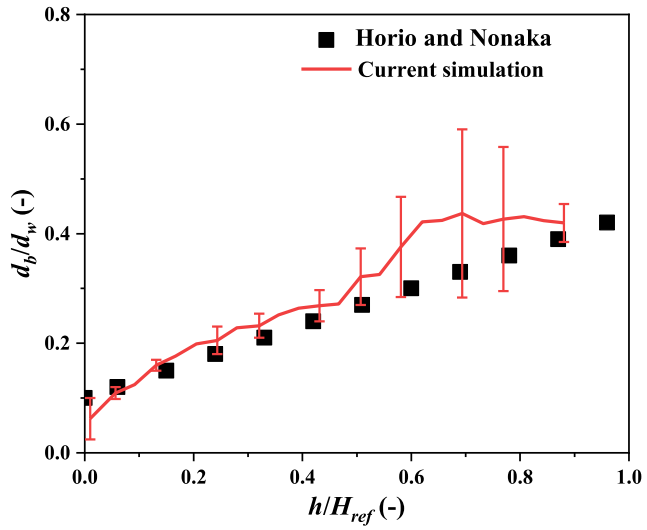

Fig. 4. Comparison of time-averaged bubble size between the simulation results and empirical correlations.

4.1.1. Bubble dynamics in a BFB

The bubble identification algorithm is validated with the empirical correlation proposed by Horio and Nonaka [46] in terms of time-averaged bubble size (d_b) along with bed height. The time-averaged operation and its standard deviation (also error bar in this work) of a quantity (ξ) are given by:

$$\xi_{ave} = \frac{1}{n}\sum_{j=1}^{n}\xi_j \tag{29}$$

$$\xi_{std} = \sqrt{\frac{1}{n}\sum_{j=1}^{n}\left(\xi_{ave}-\xi_j\right)^2} \tag{30}$$

where ξ_j is the instantaneous value of the quantity. ξ_{ave} is the time-averaged value of the quantity. ξ_{std} is the standard deviation of the time-averaged operation. n is the sampling number of the output data. For example, if the data are saved for every 0.01 s, n has a value of 1000 during the period of 5.0–15.0 s.

As shown in Fig. 4, the time-averaged bubble size increases with the bed height in the lower region due to the bubble coalescence. At the bed surface ($h/H_{ref} > 0.7$), the increasing trend of the bubble size slows down. The results obtained by the current simulation and bubble identification algorithm are consistent with that of the empirical correlations, indicating that the bubble identification algorithm can be used to predict bubble properties.

4.1.2. Gas products from a BFB reactor

Fig. 5 illustrates the validation results of reaction kinetics. The concentrations of gas products evolve sharply at the initial time. After t = 5 s, the concentrations fluctuate around fixed values, indicating that the thermochemical behaviour in the BFB achieves a steady state. The concentrations of gas products are averaged from 5 s to 15 s and the predicted concentrations are in line with the experimental data (Fig. 5 (b)), showing the reasonability of the reaction kinetics.

4.2. Flow patterns

The flow patterns are dominated by mesoscale bubble dynamics, which is known to significantly affect microscale inter-phase/particle interactions and macroscale reactor performance. As illustrated in Fig. 6, regarding the instantaneous gas–solid flow patterns, it is noted after the hydrodynamics reaches the dynamic equilibrium state, small bubbles are randomly generated at the bottom, and these small bubbles coalesce into large bubbles during the rising process. The bubbles burst on the bed surface, and the surrounding particles are thrown to the freeboard and then descend along the walls and re-circulate.

As indicated in Fig. 6 about the voidage evolution in the BFB reactor, the whole domain can be divided into a dense region within particles and bubbles, and a freeboard region. These two regions can be generally identified by the bed expansion height, which corresponds to a specific bed height with a mean voidage of 0.8. Technically, the mean voidage at any bed height ($\varepsilon_{g,\ sec}$) is obtained by averaging the voidage of the nearest cells as follows:

$$\varepsilon_{g,sec} = \frac{1}{N_{cell}}\sum_{k=1}^{N_{cell}}\varepsilon_{g,k} \tag{31}$$

where N_{cell} is the number of nearest cells at this bed height. $\varepsilon_{g,k}$ is the voidage of the k^{th} cell.

Table 4 gives the bed expansion height under different operating parameters. A smaller particle size, a higher inlet gas velocity, and a higher operating temperature lead to a larger bed expansion height. Specifically, a smaller particle size and a higher inlet gas velocity make particles rise higher by the airflow. A lower operating temperature moves forward the exothermic methanation reaction and water–gas

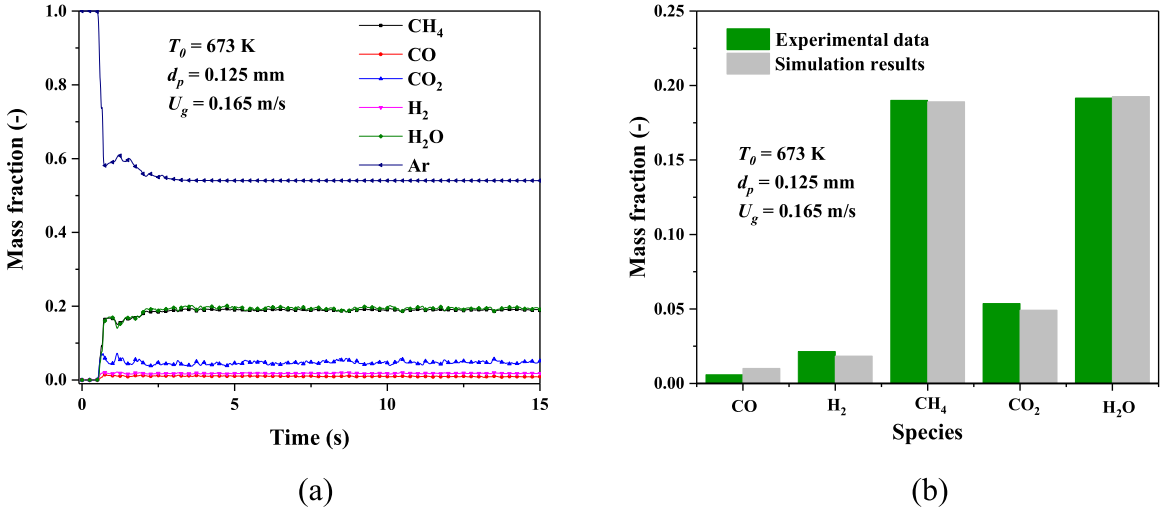

Fig. 5. (a) Time-evolution profiles of the mass fraction of gas products; (b) comparison of time-averaged mass fraction of gas products with the experimental data.

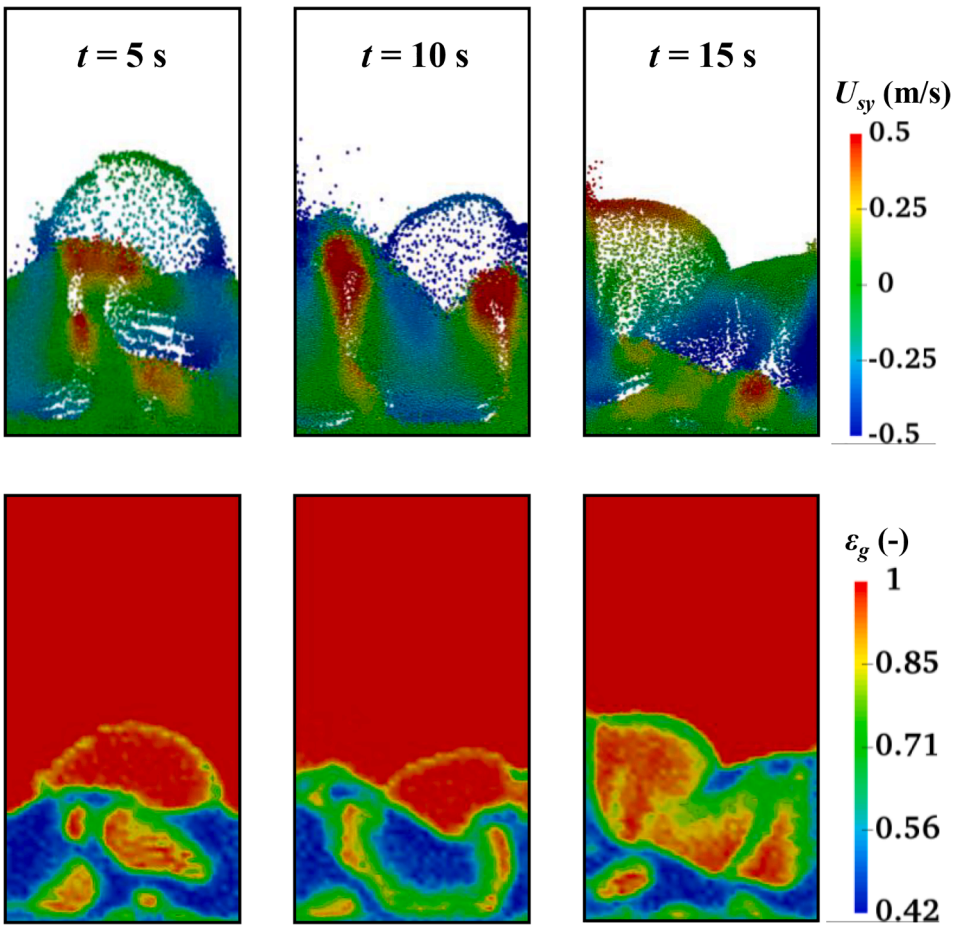

Fig. 6. Instantaneous gas–solid flow patterns, coloured by vertical particle velocity (U_{sy}) and voidage (ε_g).

Table 4
Expansion height under different operating parameters.

Case number	Parameters	Expansion height (mm)
Case 1	Base case	9.0
Case 2	$T_0 = 623$ K	8.6
Case 3	$T_0 = 723$ K	10.5
Case 4	$U_g = 0.125$ m/s	7.5
Case 5	$U_g = 0.205$ m/s	12.0
Case 6	$d_p = 0.1$ mm	10.1
Case 7	$d_p = 0.15$ mm	4.9

shift reaction, leading to a decrease in gas volume. On the contrary, a higher operating temperature causes the volume expansion of the gas phase, which enhances gas–solid momentum exchanges and increases bed expansion height.

4.3. Gas species

The instantaneous spatial distributions of gas species and reaction rates after the system reaches dynamic equilibrium are illustrated in Fig. 7 and Fig. 8, respectively. As reactants, CO and H_2 prefer to concentrate in the bottom region of the reactor, and the distribution of reaction rates is consistent with that of CO and H_2. The products of methanation reactions (i.e., CH_4 and H_2O) are mainly distributed in the upper region of the reactor, and their distributions tend to be opposite to that of CO and H_2. CO_2 is mainly distributed in the lower part of the reactor and gradually decreases along with the bed height. As a reaction product of the water–gas-shift reaction, CO_2 has an opposite spatial distribution to H_2O.

4.4. Bubble properties

Fig. 9 presents the time-evolution profiles of bubble amount (N_b) and number-averaged bubble volume (V_b) in the dynamic equilibrium state. The number-averaged bubble volume at a specific time instant is defined as:

$$V_b = \frac{1}{N_b}\sum_{k=1}^{N_b} V_{b,k} \tag{32}$$

The profiles fluctuate around fixed values over time, corresponding to the continuous bubble evolutions. Moreover, the profiles of bubble amount and bubble volume show an opposite trend. Specifically, a large bubble volume corresponds to a small bubble amount at a specific time instant. Bubble coalescence results in the increased bubble volume and reduced bubble amount.

Fig. 10 presents the time-averaged bubble amount and bubble volume under different operating parameters. The increased inlet gas velocity and decreased particle size promote the bubble motions and coalescence, which correspondingly reduces the bubble amount and enlarges the bubble volume. A higher operating temperature promotes the backward of the exothermic methanation and water–gas shift reactions, thus increasing the bubble volume and reducing the bubble amount in the bed.

4.5. Dimensionless number analysis

Particle thermophysical behaviours during the methanation process in the BFB reactor can be characterized by the dimensionless number, including particle Reynolds number (Re_p) and particle Nusselt number

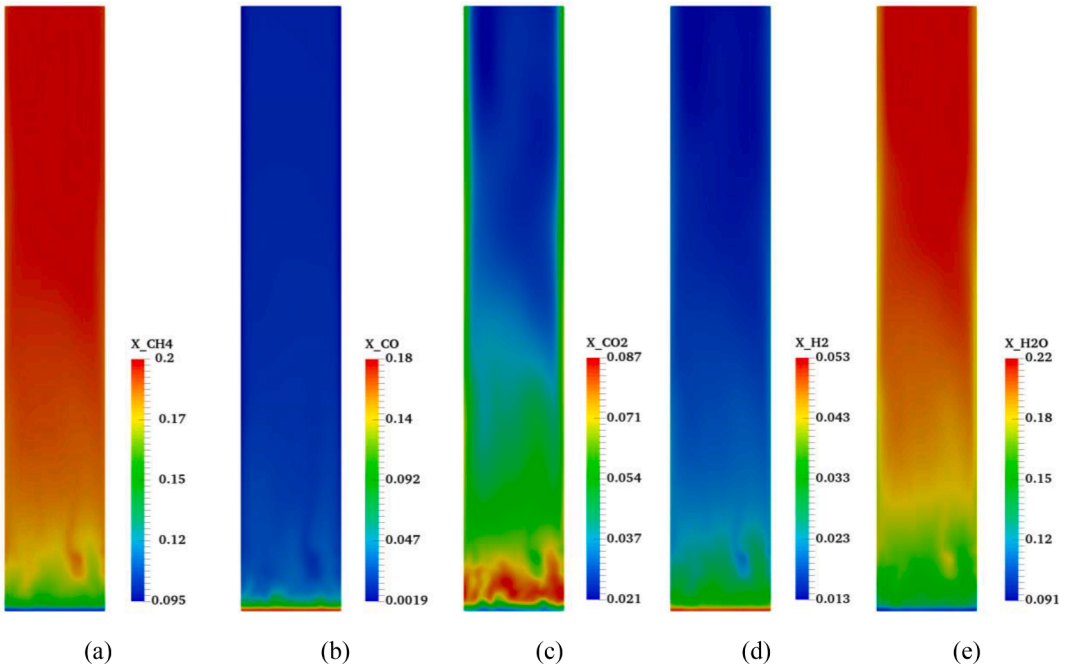

Fig. 7. Instantaneous distributions of gas species: (a) CH_4; (b) CO; (c) CO_2; (d) H_2; (e) H_2O.

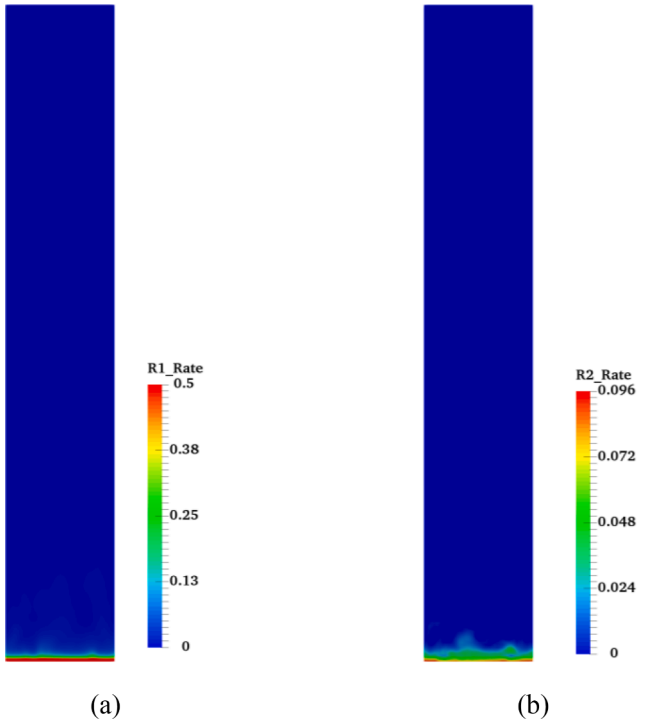

Fig. 8. Instantaneous distributions of reaction rate (kmol·m^{-3}·s^{-1}): (a) R1; (b) R2.

(Nu_p). Fig. 11 shows the relationship between the dimensionless numbers and solid holdup (ε_s) of the base case at $t = 15$ s. The size of the scattering point is proportional to the particle slip velocity. The critical values of solid holdup (i.e., 0.2 and 0.4) are used to determine three different phase states: i) the bubble phase with low solid holdup but high slip velocity; ii) the intermedia phase with medium solid holdup and slip velocity; iii) and the emulsion phase with high solid holdup and low slip velocity. Re_p decreases at the increased solid holdup because of the

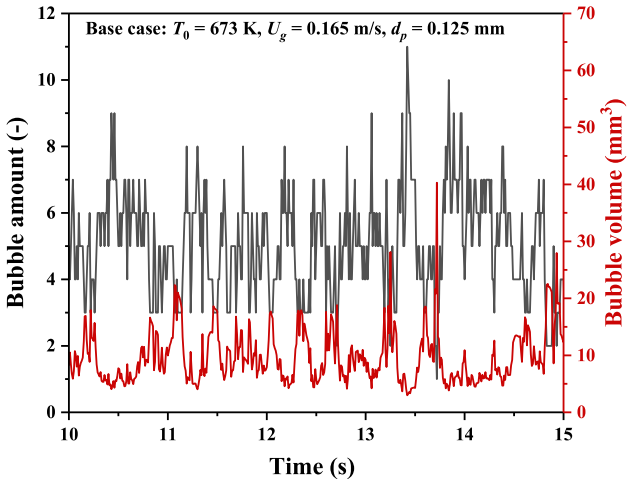

Fig. 9. Time-evolution profiles of bubble amount and number-averaged bubble volume in the BFB.

enhanced resistance of particles on the gas flow. Because of the non-linearly positive correlation between Nu_p and Re_p, Nu_p decreases with the increased solid holdup. The drag force plays a dominant role in the bubble phase, where particles have high slip velocity, Re_p, and Nu_p. On the contrary, the interparticle interactions lead to particles in the emulsion phase with smaller slip velocities, resulting in relatively small Re_p and Nu_p.

Table 5 gives the proportion of particles in the three regions (i.e., bubble phase (BP), intermedia phase (IP), and emulsion phase (EP)) and the particle-averaged Re_p and Nu_p in the three regions under different operating parameters. Under all operating conditions, Re_p and Nu_p have the maximum values in the bubble phase and the minimum value in the emulsion phase. Besides, the proportion of particles in the emulsion phase is the largest, and that in the bubble phase is the smallest. Increasing the operating temperature reduces particle amount in the bubble phase, and the Re_p and Nu_p in the bubble and emulsion phases decrease with the increase in operating temperature. A higher inlet gas

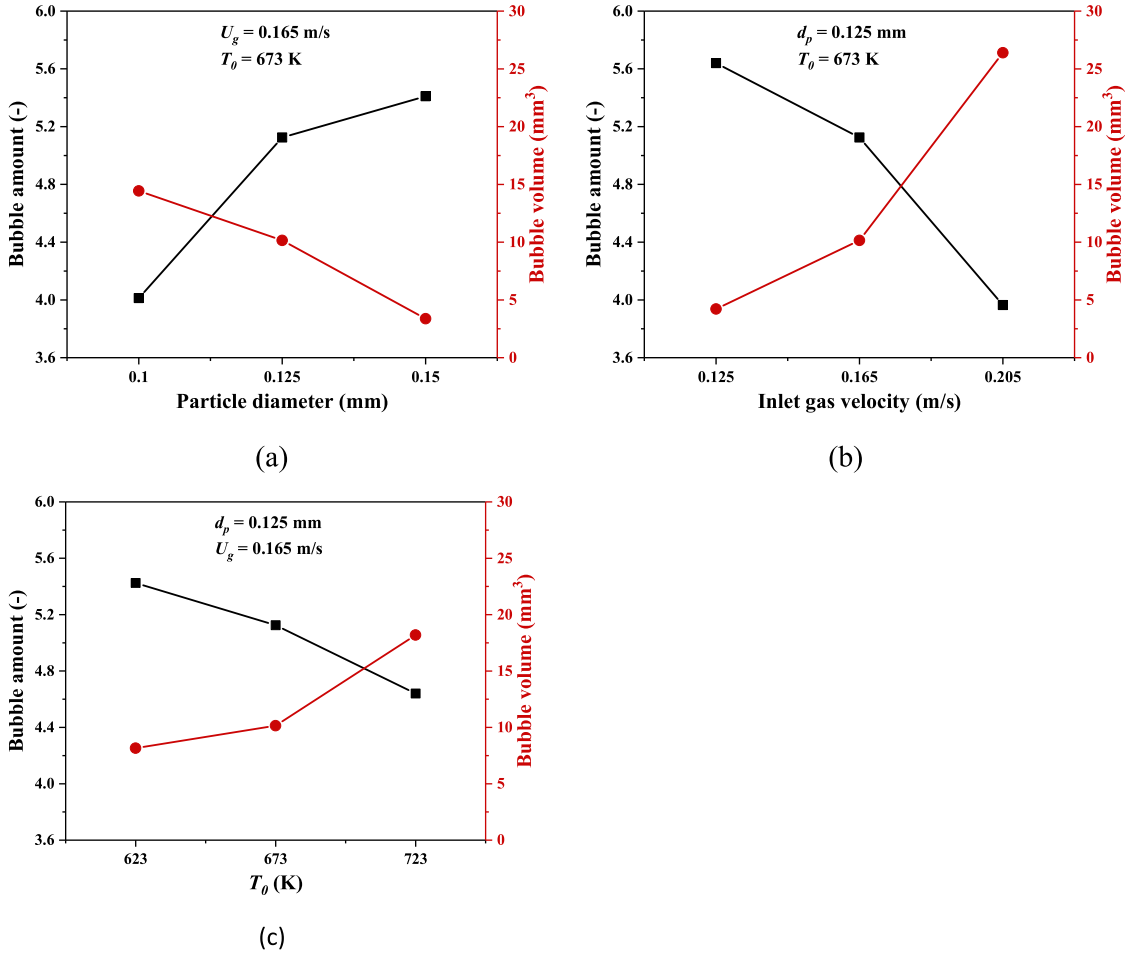

Fig. 10. Effects of operating parameters on the time-averaged bubble amount and bubble volume: (a) particle size d_p; (b) inlet gas velocity U_g; (c) operating temperature T_0.

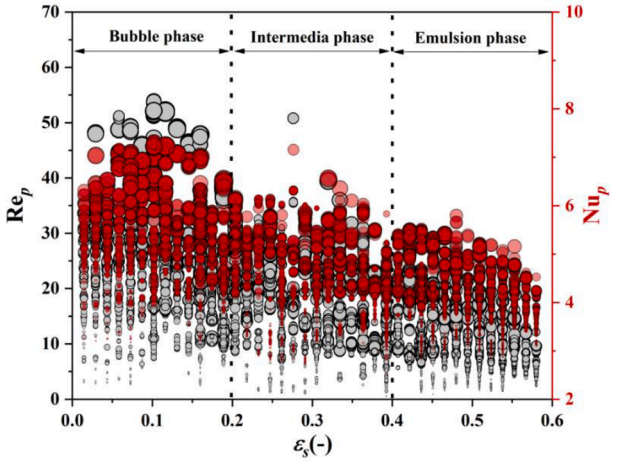

Fig. 11. Relationship between the dimensionless numbers (Re_p, Nu_p) and solid holdup (ε_s) of the base case, t = 15 s.

velocity leads to more particles entrained into the bubble phase, and the Re_p and Nu_p in the bubble phase increase, while those in the emulsion phase decrease. A larger particle size promotes Re_p and Nu_p in all regions of the BFB reactor. Increasing the particle size improves the particle proportion in the emulsion phase but reduces the particle proportion in the bubble phase.

Table 5
Number-averaged dimensionless numbers in different regions of the BFB.

Parameters	Region	The proportion of particles in each region (%)	Number-averaged Re_b (-)	Number-averaged Nu_b (-)
Base case	BP	12.6	19.17	5.18
	IP	23.2	12.51	4.6
	EP	64.2	8.21	4.0
T_0 = 623 K	BP	12.17	20.48	5.21
	IP	25.7	12.14	4.45
	EP	62.13	9.75	4.19
T_0 = 723 K	BP	9.46	18.28	5.06
	IP	27.44	11.67	4.44
	EP	63.1	8.09	4.02
U_g = 0.125 m/s	BP	4.94	17.8	4.94
	IP	18.3	12.48	4.49
	EP	76.76	8.3	4.05
U_g = 0.205 m/s	BP	21.18	19.98	5.21
	IP	36	12.5	4.48
	EP	42.82	7.67	3.94
d_p = 0.1 mm	BP	14.5	16.59	4.85
	IP	24.32	7	3.8
	EP	61.18	2.41	2.99
d_p = 0.15 mm	BP	6.38	25.64	5.57
	IP	21.52	18.45	5.04
	EP	72.1	11.56	4.4

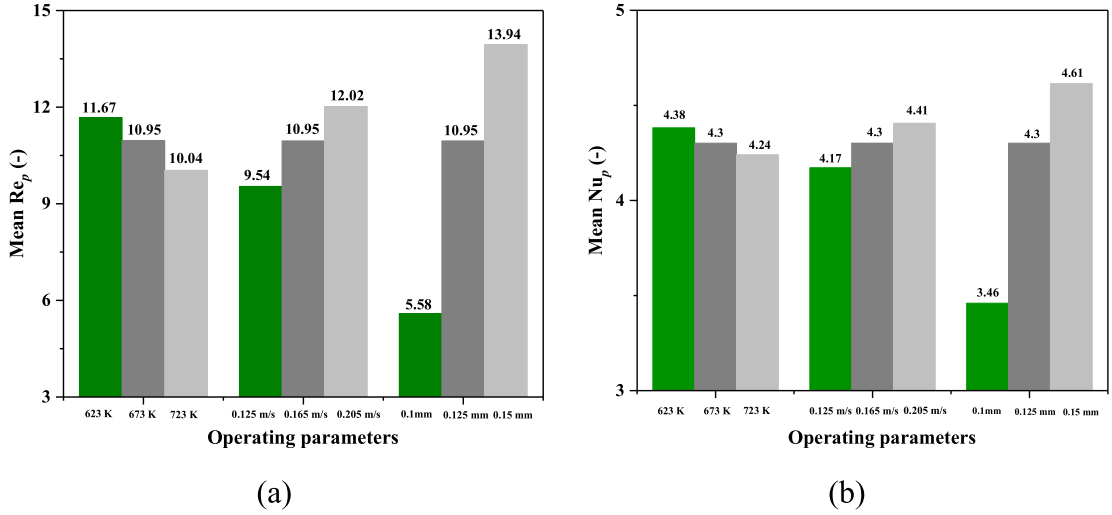

Fig. 12. Histogram distributions of number-averaged dimensionless numbers under different operating parameters: (a) Re$_p$; (b) Nu$_p$.

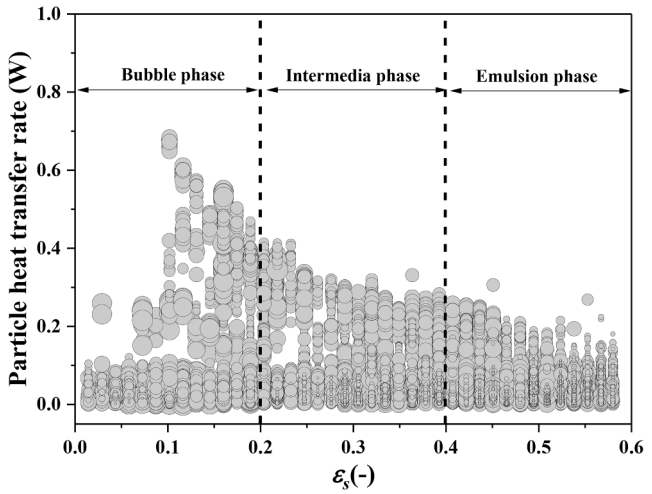

Fig. 13. Relationship between the heat transfer rate and solid holdup (ε_s) of the base case, t = 15 s.

As illustrated in Fig. 12, the Re$_p$ and Nu$_p$ after the number-averaged operation in the whole reactor show a similar trend under the varied operating parameters. A larger particle size leads to higher magnitudes of number-averaged Re$_p$ and Nu$_p$. Increasing operating temperature expands the bubble volume, leading to an increase in the proportion of particles in the intermedia and emulsion phases. Thus, more particles in the intermedia and emulsion phases decrease the number-averaged Re$_p$ and Nu$_p$ in the reactor. A higher inlet gas velocity intensifies the bed expansion, and more particles are contained in the bubble phase, which elevates the number-averaged Re$_p$ and Nu$_p$ in the reactor.

4.6. Heat and mass transfer mechanisms

Fig. 13 gives the relationship between particle heat transfer rates and solid holdup of the base case at t = 15 s. The size of the scattering point is proportional to the slip velocity. As shown in the figure, the bubble phase region has the highest heat transfer rate due to the highest inter-phase slip velocity. With the increase of solid holdup, the slip velocity between phases gradually decreases, and the heat transfer rate of particles also decreases. The emulsion phase has the smallest particle heat transfer rate.

Fig. 14 shows the effects of operating parameters on the time-averaged volume ratio of the bubble phase to the emulsion phase (B/E), the temperature difference between the bubble phase and the emulsion phase (T_{diff}), and the particle heat transfer rate. Increasing inlet gas velocity, elevating the operating temperature, and decreasing particle size lead to a larger bubble volume, a smaller bubble amount, and a higher B/E, respectively. T_{diff} is positively correlated with the B/E. With the increase in particle size and operating temperature, the variation trend of particle heat transfer rate is opposite to that of B/E, and larger B/E inhibits particle heat transfer rate. However, the particle heat transfer rate increases with the increased inlet gas velocity and is positively correlated with B/E, which is mainly due to the higher inter-phase slip velocity caused by the high inlet gas velocity. Larger-size bubbles decrease gas–solid contact efficiency, weaken inter-phase heat transfer, and intensify the bubble-to-emulsion temperature difference, which deteriorates the reaction heat removal and thus inhibits the reaction progress.

Fig. 15 shows the effects of operating parameters on the time-averaged concentration of gas products. As the particle size increases, the CH_4 concentration increases from 18.78 % to 21.3 % while the CO_2 concentration decreases from 5.34 % to 2.46 %. A higher operating temperature and inlet gas velocity decrease the CH_4 concentration but increase the CO_2 concentration. As the temperature increases from 623 K to 723 K, CH_4 concentration decreases from 20.4 % to 19.6 % but CO_2 concentration increases from 3.6 % to 4.48 %. Elevating the inlet gas velocity from 0.125 m/s to 0.205 m/s decreases CH_4 concentration decreases from 20.5 % to 19.76 % but increases CO_2 concentration from 3.5 % to 4.32 %. To summarize, a higher CH_4 concentration will be obtained at a larger particle size, a lower inlet gas velocity, and a lower operating temperature. Smaller-size bubbles and lower B/E caused by these scenarios lead to (i) improvement of gas–solid contact efficiency; (ii) more uniform distribution of temperature; (iii) enhancement of methanation reactions. Therefore, inhibiting bubble coalescence during the methanation process can effectively improve the CH_4 concentration. As the main reactants of the methanation reaction, CO and H_2 concentrations have an opposite tendency with CH_4 concentration under varied operating parameters. On the contrary, H_2O concentration shows a similar trend with CH_4 concentration under varied operating parameters. Interestingly, as the main product of the water–gas shift reaction, the variation trend of CO_2 concentration with operating parameters is opposite to that of CH_4, indicating that there is a competitive relationship between the methanation reaction and the water–gas shift reaction.

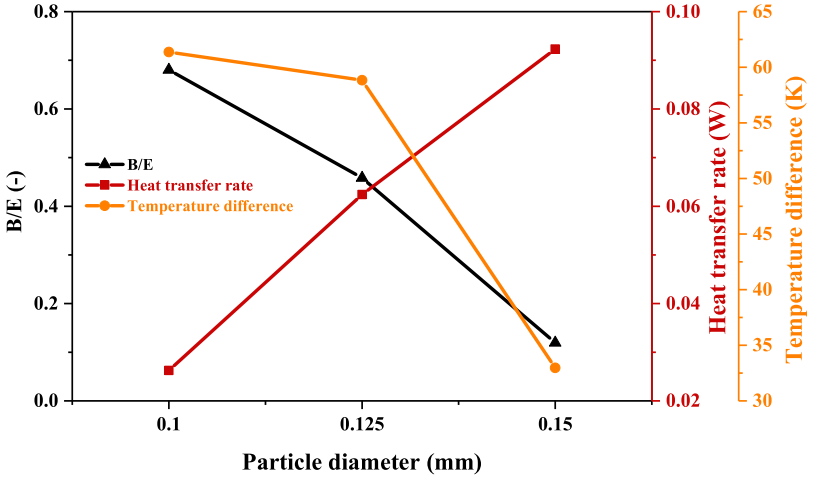

(a)

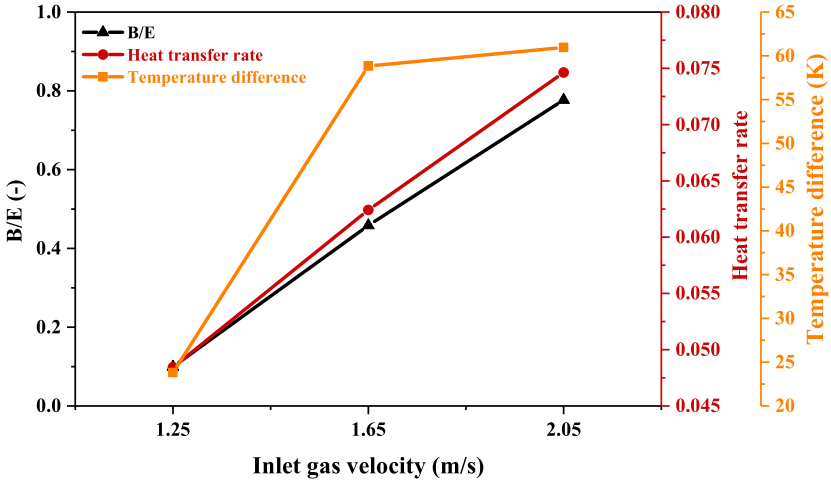

(b)

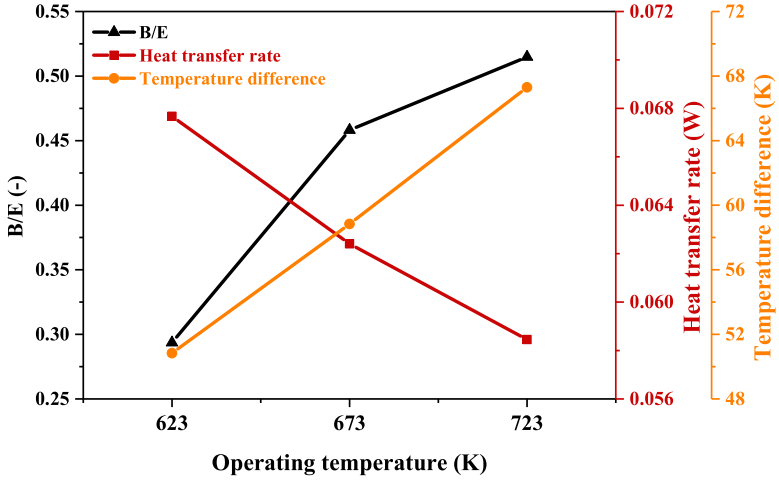

(c)

Fig. 14. Effects of operating parameters on time-averaged B/E, particle heat transfer rate and T_{diff}: (a) particle size d_p; (b) inlet gas velocity U_g; (c) operating temperature T_0.

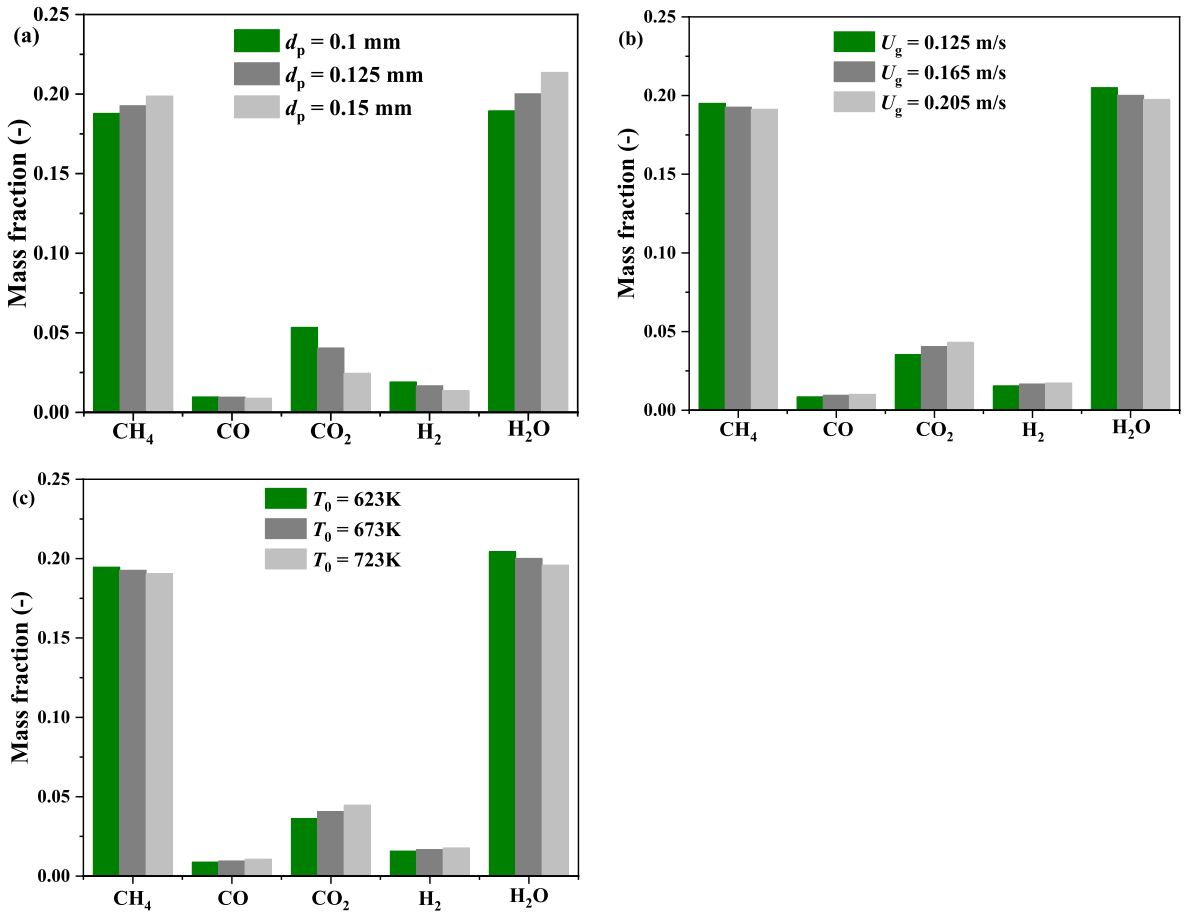

Fig. 15. Effects of operating parameters on the time-averaged concentration of gas products: (a) particle size d_p; (b) inlet gas velocity U_g; (c) operating temperature T_0.

5. Conclusion

In this study, methanation in a BFB reactor is numerically studied via the CFD-DEM approach, with a focus on mesoscale bubble dynamics. A novel bubble identification algorithm is developed for bubble identification and related property statistics. The effects of key operating parameters on the bubble properties are studied and the relationship between bubbles and reactor thermochemical characteristics is revealed. The conclusions are as follows:

1) The bubble dynamics can be well captured by the novel bubble identification algorithm. After the hydrodynamics reaches a stable state in the BFB, the evolution trend of bubble amount and bubble volume over time is opposite, and a large bubble volume corresponds to a small bubble amount. Bubble coalescence is completed near the bed surface.
2) Increasing inlet gas velocity and lowering particle size enhances the kinematics and coalescence of bubbles, thereby reducing the bubble amount and enlarging the bubble volume. Increasing the operating temperature weakens the progress of the reactions and prevents the reduction of gas volume in the bed. The gas phase accordingly has a smaller shrinkage, leading to a larger bubble volume, and a smaller bubble amount.
3) Re_p and Nu_p have the highest value in the bubble phase and the lowest value in the emulsion phase. Due to the higher inter-phase slip velocity, the bubble phase region has the highest heat transfer rate. Larger-size bubbles decrease gas–solid contact efficiency, weaken inter-phase heat transfer, and intensify the bubble-to-emulsion temperature difference, which deteriorates the reaction heat removal and thus inhibits the reaction progress. Inhibiting bubble coalescence during the methanation process in the BFB can effectively improve the heat transfer process and promote CH_4 production.

Declaration of Competing Interest

The authors declare that they have no known competing financial interests or personal relationships that could have appeared to influence the work reported in this paper.

Data availability

Data will be made available on request.

Acknowledgment

We acknowledged the support from the National Natural Science Foundation of China (No. 51806192) and Fundamental Research Funds for the Central Universities (2022ZFJH004).

References

[1] Chirone R, Paulillo A, Coppola A, Scala F. Carbon capture and utilization via calcium looping, sorption enhanced methanation and green hydrogen: a techno-economic analysis and life cycle assessment study. Fuel 2022;328:125255.
[2] Zhang D, He H, Ren Y, Haider R, Urynowicz M, Fallgren PH, et al. A mini review on biotransformation of coal to methane by enhancement of chemical pretreatment. Fuel 2022;308:121961.
[3] Rönsch S, Schneider J, Matthischke S, Schlüter M, Götz M, Lefebvre J, et al. Review on methanation–from fundamentals to current projects. Fuel 2016;166:276–96.

[4] Ngo SI, Lim Y, Lee D, Go KS, Seo MW. Flow behaviors, reaction kinetics, and optimal design of fixed-and fluidized-beds for co2 methanation. Fuel 2020;275:117886.
[5] Kopyscinski J, Schildhauer TJ, Biollaz SM. Methanation in a fluidized bed reactor with high initial co partial pressure: part i—experimental investigation of hydrodynamics, mass transfer effects, and carbon deposition. Chem Eng Sci 2011;66(5):924–34.
[6] Ostermeier P, Fischer F, Fendt S, Deyoung S, Spliethoff H. Coarse-grained cfd-dem simulation of biomass gasification in a fluidized bed reactor. Fuel 2019;255:115790.
[7] Liu Y, Hinrichsen O. Cfd simulation of hydrodynamics and methanation reactions in a fluidized-bed reactor for the production of synthetic natural gas. Ind Eng Chem Res 2014;53(22):9348–56.
[8] Wang S, Luo K, Hu C, Sun L, Fan J. Effect of superficial gas velocity on solid behaviors in a full-loop cfb. Powder Technol 2018;333:91–105.
[9] Wang S, Shen Y. Cfd-dem study of biomass gasification in a fluidized bed reactor: effects of key operating parameters. Renew Energ 2020;159:1146–64.
[10] Hu C, Luo K, Zhou M, Lin J, Kong D, Fan J. Influences of secondary gas injection pattern on fluidized bed combustion process: a cfd-dem study. Fuel 2020;268:117314.
[11] Kong D, Wang S, Zhou M, Luo K, Hu C, Li D, et al. Three-dimensional full-loop numerical simulation of co-combustion of coal and refuse derived fuel in a pilot-scale circulating fluidized bed boiler. Chem Eng Sci 2020;220:115612.
[12] Garg R, Galvin J, Li T, Pannala S. Documentation of open-source mfix–dem software for gas–solids flows. From URL https://mfix. netl. doe. gov/download/mfix/mfix_current_documentation/dem_doc_2012-1. pdf 2012.
[13] Taghipour F, Ellis N, Wong C. Experimental and computational study of gas–solid fluidized bed hydrodynamics. Chem Eng Sci 2005;60(24):6857–67.
[14] Wang X, Jin B, Zhong W. Three-dimensional simulation of fluidized bed coal gasification. Chem Eng Process 2009;48(2):695–705.
[15] Kong D, Luo K, Wang S, Yu J, Fan J. Particle behaviours of biomass gasification in a bubbling fluidized bed. Chem Eng J 2022;428:131847.
[16] Wang S, Luo K, Yang S, Hu C, Fan J. Parallel les-dem simulation of dense flows in fluidized beds. Appl Therm Eng 2017;111:1523–35.
[17] Lin J, Luo K, Wang S, Sun L, Fan J. Particle-scale study of coal-direct chemical looping combustion (clc). Energy 2022;250:123859.
[18] Wang S, Shen Y. Particle-scale study of heat and mass transfer in a bubbling fluidised bed. Chem Eng Sci 2021;240:116655.
[19] Wang S, Luo K, Fan J. Cfd-dem coupled with thermochemical sub-models for biomass gasification: validation and sensitivity analysis. Chem Eng Sci 2020;217:115550. https://https://doi.org/10.1016/j.ces.2020.115550.
[20] Wang S, Luo K, Hu C, Lin J, Fan J. Cfd-dem simulation of heat transfer in fluidized beds: model verification, validation, and application. Chem Eng Sci 2019;197:280–95.
[21] Hwang IS, Sohn J, Do Lee U, Hwang J. Cfd-dem simulation of air-blown gasification of biomass in a bubbling fluidized bed gasifier: effects of equivalence ratio and fluidization number. Energy 2021;219:119533.
[22] Hu C, Luo K, Wang S, Sun L, Fan J. Influences of operating parameters on the fluidized bed coal gasification process: a coarse-grained cfd-dem study. Chem Eng Sci 2019;195:693–706.
[23] Zhang C, Li P, Lei C, Qian W, Wei F. Experimental study of non-uniform bubble growth in deep fluidized beds. Chem Eng Sci 2018;176:515–23.
[24] Penn A, Boyce CM, Prüssmann KP, Müller CR. Regimes of jetting and bubbling in a fluidized bed studied using real-time magnetic resonance imaging. Chem Eng J 2020;383:123185.
[25] Yang S, Zhou T, Wei Y, Hu J, Wang H. Dynamical and thermal property of rising bubbles in the bubbling fluidized biomass gasifier with wide particle size distribution. Appl Energ 2020;259:114178.
[26] Gidaspow D. Multiphase flow and fluidization: continuum and kinetic theory description. J Non-Newton Fluid 1994;55(2):207–8.
[27] Ranz WE, Marshall WR. Evaporation from droplets. Chem Eng Prog 1952;48(3):141–6.
[28] Li J, Mason DJ. A computational investigation of transient heat transfer in pneumatic transport of granular particles. Powder Technol 2000;112(3):273–82.
[29] Gunn DJ. Transfer of heat or mass to particles in fixed and fluidised beds. Int J Heat Mass Tran 1978;21(4):467–76.
[30] Garcia-Gutierrez LM, Hernández-Jiménez F, Cano-Pleite E, Soria-Verdugo A. Experimental evaluation of the convection heat transfer coefficient of large particles moving freely in a fluidized bed reactor. Int J Heat Mass Tran 2020;153:119612.
[31] Lian G, Zhong W. Cfd–dem modeling of oxy-char combustion in a fluidized bed. Powder Technol 2022;407:117698.
[32] Li J, Agarwal RK, Zhou L, Yang B. Investigation of a bubbling fluidized bed methanation reactor by using cfd-dem and approximate image processing method. Chem Eng Sci 2019;207:1107–20.
[33] Gao X, Yu J, Lu L, Rogers WA. Coupling particle scale model and superdem-cfd for multiscale simulation of biomass pyrolysis in a packed bed pyrolyzer. Aiche J 2021;67(4):e17139.
[34] Lu L, Gao X, Gel A, Wiggins GM, Crowley M, Pecha B, et al. Investigating biomass composition and size effects on fast pyrolysis using global sensitivity analysis and cfd simulations. Chem Eng J 2021;421:127789.
[35] Zhou Z, Yu AB, Zulli P. Particle scale study of heat transfer in packed and bubbling fluidized beds. Aiche J 2009;55(4):868–84.
[36] Li J, Yang B. Bubbling fluidized bed methanation study with resolving the mesoscale structure effects. Aiche J 2019;65(5):e16561.
[37] Li J, Yang B. Multi-scale cfd simulations of bubbling fluidized bed methanation process. Chem Eng J 2019;377:119818.
[38] Li T, Dietiker J, Zhang Y, Shahnam M. Cartesian grid simulations of bubbling fluidized beds with a horizontal tube bundle. Chem Eng Sci 2011;66(23):6220–31.
[39] Lu L, Konan A, Benyahia S. Influence of grid resolution, parcel size and drag models on bubbling fluidized bed simulation. Chem Eng J 2017;326:627–39.
[40] Laverman JA, Roghair I, Annaland MVS, Kuipers H. Investigation into the hydrodynamics of gas–solid fluidized beds using particle image velocimetry coupled with digital image analysis. Can J Chem Eng 2008;86(3):523–35.
[41] Wang S, Luo K, Hu C, Sun L, Fan J. Impact of operating parameters on biomass gasification in a fluidized bed reactor: an eulerian-lagrangian approach. Powder Technol 2018;333:304–16.
[42] Cardoso J, Silva V, Eusébio D, Brito P, Boloy RM, Tarelho L, et al. Comparative 2d and 3d analysis on the hydrodynamics behaviour during biomass gasification in a pilot-scale fluidized bed reactor. Renew Energ 2019;131:713–29.
[43] Clarke DA, Sederman AJ, Gladden LF, Holland DJ. Investigation of void fraction schemes for use with cfd-dem simulations of fluidized beds. Ind Eng Chem Res 2018;57(8):3002–13.
[44] Bird RB. Transport phenomena. Appl Mech Rev 2002;55(1):R1–4.
[45] Burcat A, Ruscic B. Third millenium ideal gas and condensed phase thermochemical database for combustion (with update from active thermochemical tables).: Argonne National Lab.(ANL), Argonne, IL (United States); 2005.
[46] Horio M, Nonaka A. A generalized bubble diameter correlation for gas-solid fluidized beds. Aiche J 1987;33(11):1865–72.